

The overlooked NIR luminescence of Cr(ppy)₃

Laura Stein, Pit Boden, Robert Naumann, Christoph Förster, Gereon Niedner-Schatteburg and Katja Heinze

Supplementary Information

General. All reagents were used as received from commercial suppliers (ABCR, Acros Organics, Alfa Aesar, Fischer, Sigma-Aldrich and TCI). THF and toluene were refluxed over potassium and distilled under argon prior to use. Dichloromethane was dried and distilled from calcium hydride under argon prior to use. All reactions and measurements were performed under argon and waterfree atmosphere unless otherwise noted. A glovebox (UniLab/MBraun – Ar 4.8, O₂ < 1 ppm, H₂O < 0.1 ppm) was used to store and weigh sensitive compounds for synthesis as well as to prepare any sample that required absence of oxygen and water.

FD mass spectra were recorded on a *Thermo Fischer DFS* mass spectrometer.

IR spectra were recorded on a *Bruker Alpha II* FTIR spectrometer with an ATR unit containing a diamond crystal.

Elemental analyses were performed by the central analytic service of the department of chemistry of the University of Mainz using an *vario EL Cube* from *Elementar*.

Electrochemical experiments were carried out on a *BioLogic SP-200* voltammetric analyzer using platinum wires as counter and working electrodes and 0.01 M Ag/AgNO₃ as the reference electrode. The measurements were carried out at a scan rate of 100 mV s⁻¹ for cyclic voltammetry experiments using 0.1 M [nBu₄N][PF₆] as supporting electrolyte and 0.001 M of the sample in dichloromethane. Potentials are referenced relative to the ferrocene/ferrocenium couple.

UV/Vis absorption spectra in solution were recorded on a *Jasco V770* spectrometer using 1.0 cm quartz cells with a Schott valve to maintain an inert atmosphere.

Steady-state irradiation was carried out with an *Asahi-MAX-303* Xe lamp (300 W), together with 420±5 nm filters. The samples were prepared under inert conditions in 1.0 cm quartz cells with a Schott valve. UV/Vis spectra were recorded after the indicated time intervals.

Emission spectra and luminescence decay curves (solutions and powder samples) were recorded with a *FLS1000 spectrometer* from *Edinburgh Instruments* equipped with the cooled red and NIR sensitive photomultiplier detectors PMT-980 and N-G09 PMT-1700, together covering the whole spectral range between 200 nm and 1700 nm. A xenon arc lamp Xe2 (450 W) was used for excitation in steady-state measurements. Time-resolved luminescence experiments were performed in the multi-channel scaling mode employing the µs-xenon-flashlamp *mF2* (pulse width ca. 2 µs) as excitation source. Measurements at low temperature were conducted using a liquid nitrogen cooled cryostat *Optistat* from *Edinburgh Instruments*. Absolute luminescence quantum yields Φ were determined using an integrating sphere from *Edinburgh Instruments*. Relative uncertainty of Φ is estimated to be ±20 %.

Transient absorption spectroscopy experiments were conducted using a *LP980KS* setup from *Edinburgh Instruments* equipped with a Nano LG 300-10 Nd:YAG laser from *Litron* (ca. 5 ns pulse width). The frequency-tripled output with a wavelength of 355 nm was employed for the excitation (30 mJ pulse energy). To ensure homogeneous excitation of the whole observation volume (10 mm × 10 mm quartz cuvette) the beam was brought to a diameter of 1.2 cm using a beam expander. The transient absorption spectra were recorded with an integration time of 100 ns using an iCCD camera

from *Andor*. For the detection of the decay traces at single wavelengths a photomultiplier tube was employed. All transient absorption experiments were performed at 293 K.

KBr pellets were prepared by mixing neat powder of the compound (0.7 – 1.6 mg, depending on the experiment) with dry KBr (180 – 300 mg, stored in a compartment dryer at 80 °C, purchased from Merck) and grinding to a homogenous mixture. This mixture was filled in an evacuable pellet die with a diameter of 13 mm and sintered at a pressure of 0.75 GPa. Please consider the respective sections for more details on the specific sample preparations.

UV/VIS absorption spectroscopy in the solid state (KBr pellets) was performed with a *Lambda 900* UV/VIS spectrometer equipped with a diffuse reflectance accessory (*Harrick Praying Mantis*). The powder samples were prepared by mixing neat powder of the compound with dry KBr in a ratio of ca. 1:100 and grinding to a homogenous mixture.

Temperature-dependent steady state NIR luminescence measurements (KBr pellets) were conducted on a *Horiba Jobin Yvon Fluorolog 3-22 τ* spectrometer equipped with a 450 W Xenon lamp and a *DSS – IGA020L* NIR detector (850 nm $\leq \lambda_{em} \leq$ 1550 nm). Spectral selection was realized with double and single grating monochromators in the excitation and emission paths, respectively (excitation: 1200 grooves/mm; near-IR emission 600 grooves/mm). A combination of two long-pass filters (*FELH0500 Thorlabs*, transmission \geq 92% above 500 nm and *FELH0850 Thorlabs*, transmission \geq 90% above 860 nm) was used in the emission channel to avoid higher order excitation light. All emission spectra presented were corrected for the wavelength-dependent sensitivity of the detector. KBr pellets were prepared as described in the section on the preparation of KBr pellets using 0.7 mg of sample and 180 mg of KBr. Temperature-dependent experiments between 5 K and 290 K were performed using a closed-cycle helium cryostat (*ColdEdge, 101J cryocooler*) to cool down the sample. The cryocooler was equipped with a pellet holder (copper) and CaF₂ windows.

NIR luminescence quantum yields (KBr pellets) were determined in analogy to the procedures described by Wrighton et al. and later Liu et al., who measured fluorescence quantum yields with a conventional fluorescence spectrometer.^{1,2} All spectra were recorded at room temperature on the *Horiba Jobin Yvon Fluorolog 3-22 τ* spectrometer (see the sections on static NIR luminescence spectroscopy for more details) with the KBr pellets being mounted in a solid state sample holder. The absorption of the complex was measured by considering the difference in area between the excitation light ($\lambda_{exc} = 350$ nm) scattered by a neat KBr pellet (J_0) and a pellet containing the complex (J). For the luminescence the area J_f under the emission curve was considered. The quantum yields were measured relative to the standard Yb(tta)₃(H₂O)₂ with $\phi_r(Yb) = 0.55$ % as PMMA film.³ The NIR photoluminescence quantum yield was calculated according to the following equation, where the abbreviation S stands for the investigated sample with unknown quantum yield and Yb represents the reference Yb(tta)₃(H₂O)₂:

$$\phi_{NIR} = \frac{J_0 - J(Yb)}{J_0 - J(S)} \cdot \frac{J_f(S)}{J_f(Yb)} \cdot \phi_r(Yb)$$

The error bars for the photoluminescence quantum yields are estimated to ± 25 % for the applied procedures according to the literature.¹

Time-resolved step-scan FTIR experiments (KBr pellets) were performed with the FTIR spectrometer *Bruker Vertex 80v*, operated in the step-scan mode. A liquid-nitrogen-cooled mercury cadmium telluride (MCT) detector (*Kolmar Tech., Model KV100-1-B-7/190*) with a rise time of 25 ns, connected to a fast preamplifier and a 14-bit transient recorder board (*Spectrum Germany, M3I4142, 400 MS/s*), was used for signal detection and processing. The laser setup used for the measurements includes a

Q-switched Nd:YAG laser (*Innolas SpitLight Evo I*) generating pulses with a duration of about 6 ns at a repetition rate of 100 Hz. The third harmonic (355 nm) of the Nd:YAG laser was used directly for sample excitation. The UV pump beam was attenuated to about 2.0 mJ per shot at a diameter of 9 mm. The beam was directed onto the sample and adjusted to have a maximal overlap with the IR beam of the spectrometer. The sample chamber was equipped with anti-reflection-coated germanium filters to prevent the entrance of laser radiation into the detector and interferometer compartments.

The KBr pellets were prepared as described in the section on luminescence spectroscopy (ca. 0.7 mg of the complex and ca. 180 mg KBr). The strongest peak in the ground state spectrum showed an absorption of about 0.6 OD with the mentioned concentration. The measurements were performed at a constant temperature of 20 K using a closed-cycle helium cryostat (*ARS Model DE-202A*). The cryocooler was equipped with a pellet holder and CaF₂ windows.

The temporal resolution of the 14-bit transient recorder board was chosen to 50 ns and 10000 time slices were recorded to cover a time range of 500 μ s. The time when the laser pulse reached the sample was set as zero point in all spectra. The time delay between the start of the experiment and the laser pulse was controlled with a *Stanford Research Systems DG535* delay generator and set to 1.3 μ s before the laser excitation of the sample. The spectral region was limited by undersampling to 988 – 1975 cm⁻¹ with a spectral resolution of 4 cm⁻¹ resulting in 555 interferogram points. An IR broad band filter (850 – 1750 cm⁻¹) and the CaF₂ windows (no IR transmission < 1000 cm⁻¹) of the cryostat prevented problems when performing a Fourier transformation (i.e. no IR intensity outside the measured region should be observed). FTIR ground state spectra were recorded systematically to check if there is no sample degradation. The error for the excited state lifetime is estimated to ± 10 %.

Crystal Structure Determination. Intensity data for crystal structure determination of *fac*-Cr(ppy)₃ were collected with a STADIVARI diffractometer from STOE & CIE GmbH using Mo-K α radiation (λ = 0.71073 Å). The diffraction frames were integrated using the STOE X-Area software package⁴ and were corrected for absorption with STOE LANA^{5,6} of the STOE X-Area software package.⁴ The structures were solved with SHELXT⁷ and refined by the full-matrix method based on F^2 using SHELXL⁸ of the SHELX⁹ software package and the ShelXle¹⁰ graphical interface. All non-hydrogen atoms were refined anisotropically while the positions of all hydrogen atoms were generated with appropriate geometric constraints and allowed to ride on their respective parent atoms with fixed isotropic thermal parameters. Crystallographic data for the structure reported in this paper have been deposited with the Cambridge Crystallographic Data Centre as supplementary publication no. CCDC-2124885.

Crystallographic Data of *fac*-Cr(ppy)₃. C₃₃H₂₄CrN₃ (514.55); tetragonal; $P\bar{4}2_1c$; a = 23.0243(3) Å, b = 23.0243(3) Å, c = 9.21690(10) Å, α = 90°, β = 90°, γ = 90°; V = 4886.05(14) Å³; Z = 8; density (calculated) 1.399 g cm⁻³, T = 120(2) K, μ = 0.497 mm⁻¹, $F(000)$ = 2136; crystal size 0.090 x 0.069 x 0.058 mm³; θ = 1.978 to 29.750 deg.; $-31 \leq h \leq 29$, $-31 \leq k \leq 32$, $-11 \leq l \leq 12$; rfln collected = 49789; rfln unique = 6346 [$R(\text{int})$ = 0.0241]; completeness to θ = 25.242 deg. = 99.4 %; semi empirical absorption correction from equivalents; max. and min. transmission 0.9697 and 0.4753; data 6346; restraints 0, parameters 334; goodness-of-fit on F^2 = 1.009, final indices [$I > 2\sigma(I)$] R_1 = 0.0263, wR_2 = 0.0647; R indices (all data) R_1 = 0.0300, wR_2 = 0.0652; largest diff. peak and hole 0.259 and -0.427 e Å⁻³.

Density functional theory and CASSCF-NEVPT2 calculations were carried out using the ORCA program package 5.0.1.¹¹

DFT calculations were performed using the B3LYP functional^{12,13} employing the RIJCOSX approximation.^{14,15} Tight convergence criteria were chosen for DFT-UKS calculations (keywords *tightscf* and *tightopt*). Relativistic effects were calculated at the zeroth order regular approximation (ZORA) level.¹⁶ The ZORA keyword automatically invokes relativistically adjusted basis sets. To account for

solvent effects, a conductor-like screening model (CPCM) modeling acetonitrile was used in all calculations.^{17,18} Geometry optimizations were performed using Ahlrichs' polarized valence triple- ζ basis set (def2-TZVPP).^{19,20} Atompairwise dispersion correction was performed with the Becke-Johnson damping scheme (D3BJ).^{21,22} The energy of the electronic states and the presence of energy minima were checked by numerical frequency calculations. Explicit counter ions and/or solvent molecules were not taken into account. TD-DFT calculations were performed at the same level of theory. Fifty vertical spin-allowed transitions were calculated. The assignment of the state characters has been done dividing the molecule into four fragments (metal center and three ppy⁻ ligands) and calculating charge transfer (CT) numbers, as implemented in the TheoDore software package.^{23,24}

CASSCF(7,12)-FIC-NEVPT2 calculations were performed at the DFT-optimized ground state geometry using the complete-active-space self-consistent field method including spin-orbit coupling (SOC-CASSCF)^{25,26} in conjunction with the fully internally contracted N-electron valence perturbation theory to second order (FIC-NEVPT2)^{27,28} in order to recover missing dynamic electron correlation. All electronic states are classified by irreducible representations of the *O* point group, in spite of the lower actual symmetry of the considered complex. In order to accurately model the ligand field, the active space was expanded to encompass the dominant bonding/antibonding orbitals formed between chromium and the ligand. In addition to the minimal active space of (3,5), two occupied Cr–N σ bonding orbitals and a second d shell²⁹ were included in these calculations giving an active space of (7,12). 10 quartet and 10 doublet roots were calculated with this active space.

Synthesis of *fac*-Cr(ppy)₃: The precursor CrPh₃(thf)₃ was prepared according to a literature procedure.³⁰ The red product was used without further purification. *fac*-Cr(ppy)₃ was prepared according to a reported procedure from CrPh₃(thf)₃.³¹ The product was isolated as an analytically pure yellow powder. Orange crystals suitable for single crystal X-ray crystallography were obtained from concentrating a CH₂Cl₂/toluene solution. Elemental analysis. calcd. (%) for C₃₃H₂₄CrN₃ (514.57): C, 77.03; H, 4.70; N, 8.17; found: C, 77.24; H, 5.01; N, 8.09. MS (FD): *m/z* (%) = 514.396; calcd. for C₃₃H₂₄CrN₃ *m/z* (%) = 514.138. IR (ATR): $\tilde{\nu}$ = 3043 (w), 1595 (s), 1561 (m), 1469 (s), 1426 (m), 1298 (w), 1259 (m), 1168 (m), 1098 (w), 1059 (w), 1022 (w), 999 (w), 936 (vw), 878 (vw), 800 (w), 748 (vs), 732 (vs), 711 (s), 659 (m), 631 (m), 554 (w), 474 (w), 412 (m) cm⁻¹. UV-Vis (CH₂Cl₂): λ_{max} (ϵ / 10³ M⁻¹cm⁻¹): 261 (50.5), 298 (31.5), 385 (5.7), 440 (3.0) nm. CV (CH₂Cl₂, 0.1 M [ⁿBu₄N][PF₆], vs. ferrocene, 293 K): *E*_p = +0.24 V.

Table S1. Bond lengths [Å] and angles [deg] of *fac*-Cr(ppy)₃ and [Cr(bpy)₃]³⁺ from XRD measurements and DFT calculations. Intraligand and interligand angles highlighted in yellow and green, respectively.

	<i>fac</i> -Cr(ppy) ₃				[Cr(bpy) ₃] ³⁺	
	XRD	DFT quartet ground state	DFT lowest doublet state		XRD ³²	DFT quartet ground state
Cr1–N1	2.145(2)	2.146	2.138	Cr1–N1	2.042(5)	2.057
Cr1–N2	2.149(2)	2.146	2.147	Cr1–N2	2.042(5)	2.054
Cr1–N3	2.140(2)	2.146	2.153	Cr1–N3	2.042(5)	2.055
Cr1–C1	2.059(2)	2.063	2.055	Cr1–N4	2.042(5)	2.053
Cr1–C2	2.061(2)	2.063	2.053	Cr1–N5	2.042(5)	2.056
Cr1–C3	2.058(2)	2.063	2.044	Cr1–N6	2.042(5)	2.051
N1–Cr–N2	92.86(6)	93.9	93.6	N1–Cr–N2	94.6(2)	94.45
N1–Cr–N3	94.50(6)	93.9	93.3	N1–Cr–N3	94.6(2)	96.50
N1–Cr–C1	171.25(7)	172.0	171.5	N1–Cr–N4	171.0(2)	173.8
N1–Cr–C2	79.26(7)	79.3	79.4	N1–Cr–N5	79.1(2)	79.6
N1–Cr–C3	93.60(7)	90.8	91.4	N1–Cr–N6	92.3(2)	90.0
N2–Cr–N3	90.39(6)	93.9	93.7	N2–Cr–N3	94.6(2)	95.4
N2–Cr–C1	93.05(7)	90.8	90.7	N2–Cr–N4	92.3(2)	90.7
N2–Cr–C2	167.52(7)	172.0	171.9	N2–Cr–N5	171.0(2)	172.7
N2–Cr–C3	79.28(7)	79.3	79.4	N2–Cr–N6	79.1(2)	79.7
N3–Cr–C1	79.03(7)	79.3	79.1	N3–Cr–N4	79.1(2)	79.5
N3–Cr–C2	99.81(7)	90.8	90.9	N3–Cr–N5	92.3(2)	89.6
N3–Cr–C3	167.17(7)	172.0	171.9	N3–Cr–N6	171.0(2)	172.2
C1–Cr–C2	95.93(8)	96.4	96.7	N4–Cr–N5	94.6(2)	95.5
C1–Cr–C3	93.83(7)	96.4	96.6	N4–Cr–N6	94.6(2)	94.4
C2–Cr–C3	91.47(8)	96.4	96.4	N5–Cr–N6	94.6(2)	95.9

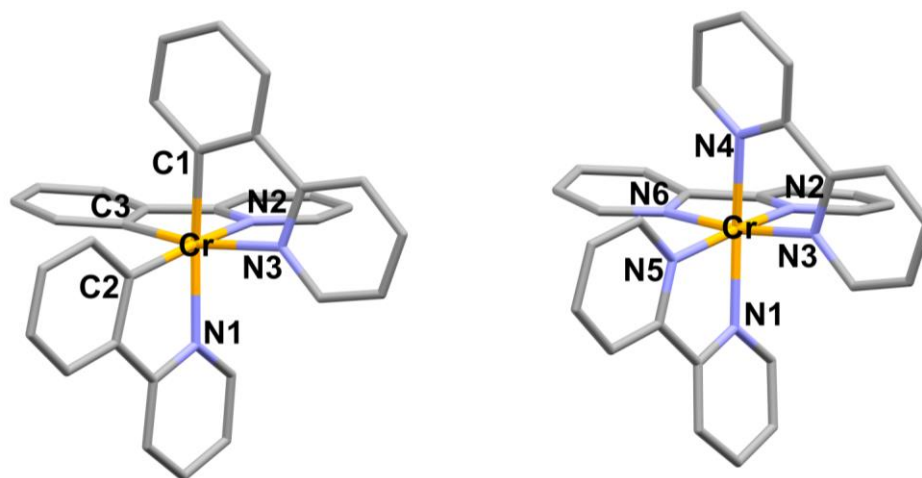


Figure S1. Molecular structures of *fac*-Cr(ppy)₃ and [Cr(bpy)₃]³⁺ ³² with atom numbering used in Table S1. Hydrogen atoms omitted for clarity.

Table S2. Shape parameters for octahedron $S(\text{OC-6})$ and trigonal prism $S(\text{TPR-6})$ of fac-Cr(ppy)_3 and $[\text{Cr(bpy)}_3]^{3+}$ from DFT calculated geometries and from XRD data.

	fac-Cr(ppy)_3		$[\text{Cr(bpy)}_3]^{3+}$	
	DFT	XRD	DFT	XRD ³²
$S(\text{OC-6})$	0.88	1.17	0.83	0.93
$S(\text{TPR-6})$	14.58	11.92	14.78	13.68

Table S3. Emission data of fac-Cr(ppy)_3 : Emission wavelength, corresponding quantum yields and excited state lifetimes at different temperatures and in different physical states. Excitation was at 420 nm, if not stated otherwise.

State/solvent	T / K	$\lambda_{\text{em}} / \text{nm}$	$\Phi / \%$	$\tau / \mu\text{s}$
2-MeTHF, Ar	293	910	-	9.5
2-MeTHF, Ar	77	890, 910 (sh), 1020 (sh)	-	48
CH_2Cl_2 , Ar ^a	293	910	0.03	9.3
Powder	293	905	0.02	10 (76 %); $\tau_2 = 3$ (24 %)
KBr pellet	298	925	0.3 ^b	-
KBr pellet	20	922	-	9.8 ^c

^a Excitation at 473 nm.

^b Relative to $\text{Yb(tta)}_2(\text{H}_2\text{O})_2$.

^c Excitation at 355 nm, from step-scan FTIR experiments.

Table S4. Emission data of $[\text{Cr(bpy)}_3][\text{PF}_6]_3$: Emission wavelength, corresponding quantum yields and excited state lifetimes.

Solvent	$\lambda_{\text{em}} / \text{nm}$	$\tau_{\text{RT}} (\tau_{\text{RT,deox}}) / \mu\text{s}$	$\tau_{\text{LT}} (\tau_{\text{LT,deox}}) / \mu\text{s}$	$\Phi_{\text{deox}} / \%$	reference
H_2O	730	52 (74)	6500 ^a	0.089	33,34
1 M HCl(aq)	729	– (69)	–	0.25 %	35

^a Aq. HClO_4 (pH = 3.1)/MeOH 1:1 v/v at 77 K.

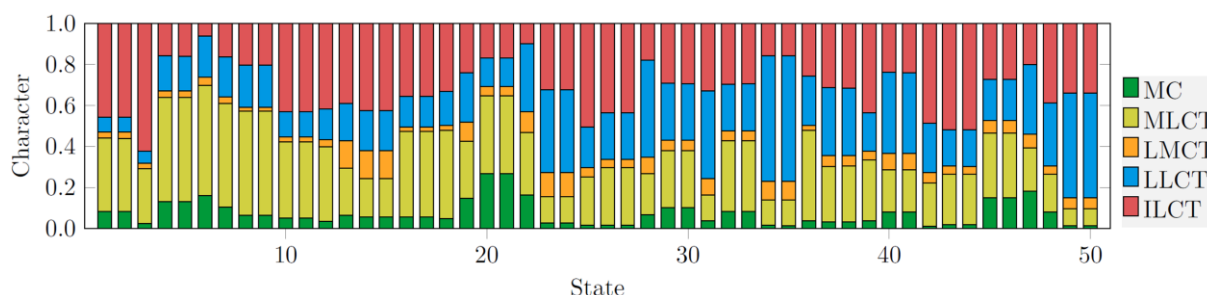
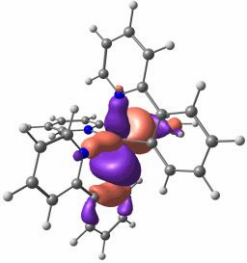
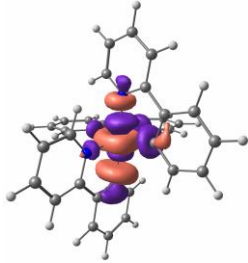
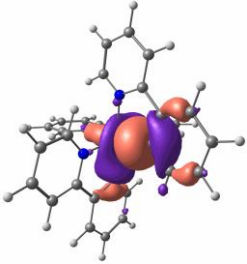
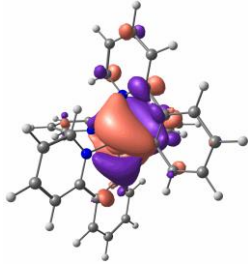
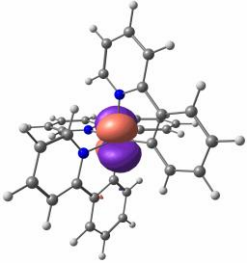
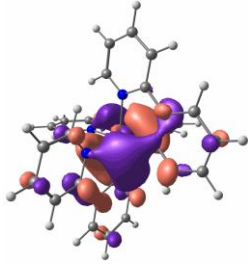
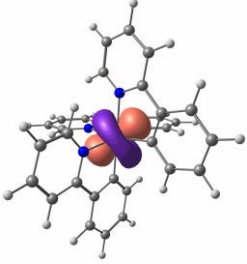
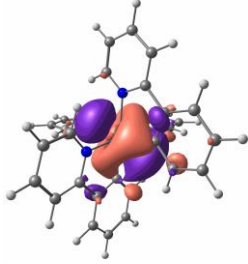
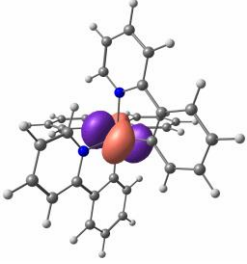
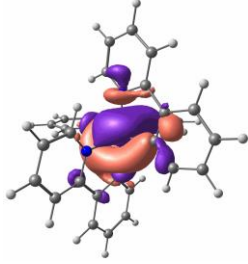
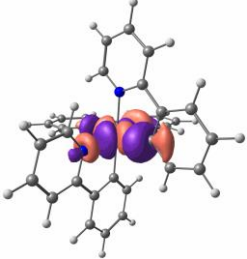
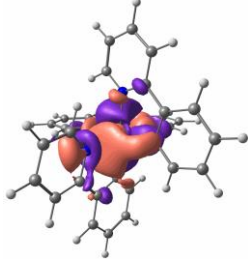


Figure S2. TD-DFT-UKS charge transfer numbers of fac-Cr(ppy)_3 defined from 0 to 1 of the lowest-lying 50 quartet states using the TheoDore software package.^{23,24}

Table S5. Orbital energies/Hartree of the canonical orbitals used in the active space of the CASSCF(7,12)-FIC-NEVPT2 calculation, depicted at a contour value of 0.03 a.u..

#	E / H	orbital	#	E / H	orbital
130	-0.373584		136	+0.257474	
131	-0.372416		137	+0.544860	
132	-0.044505		138	+0.564580	
133	-0.039633		139	+0.792775	
134	-0.019034		140	+0.963221	
135	+0.240689		141	+1.026967	

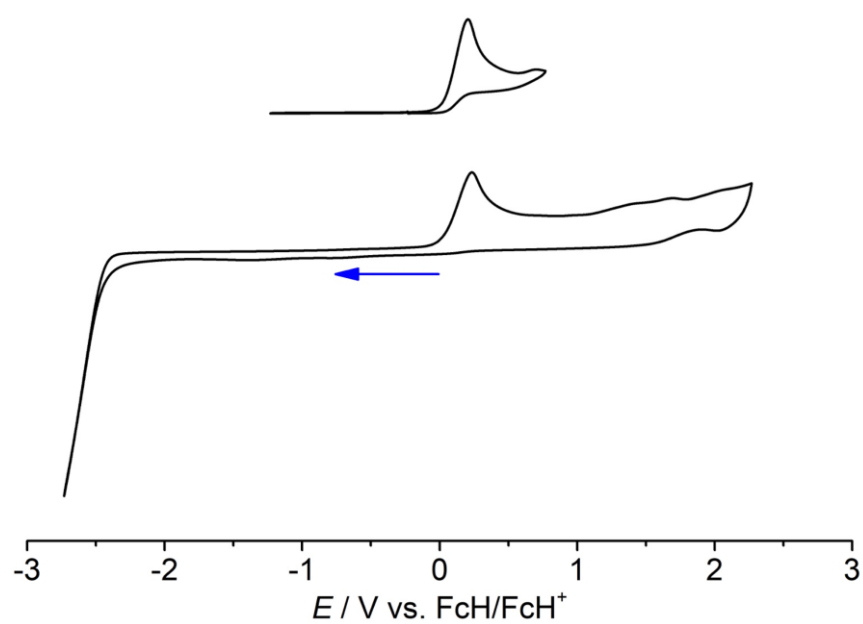


Figure S3. Cyclic voltammograms of *fac*-Cr(ppy)₃ in CH₂Cl₂/[*n*Bu₄N][PF₆]; *E* vs. ferrocene.

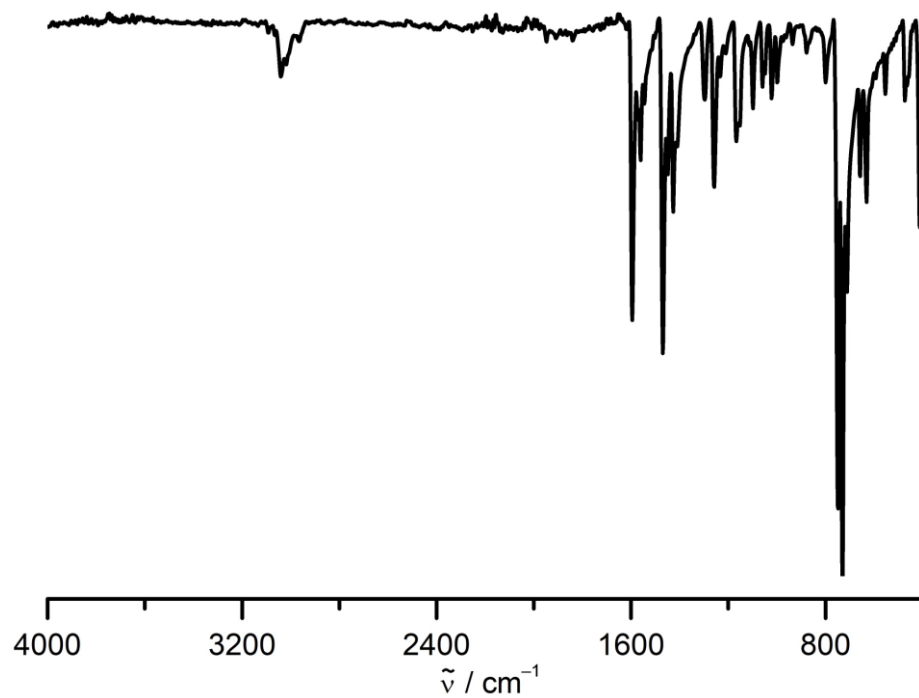


Figure S4. ATR-IR spectrum of solid *fac*-Cr(ppy)₃.

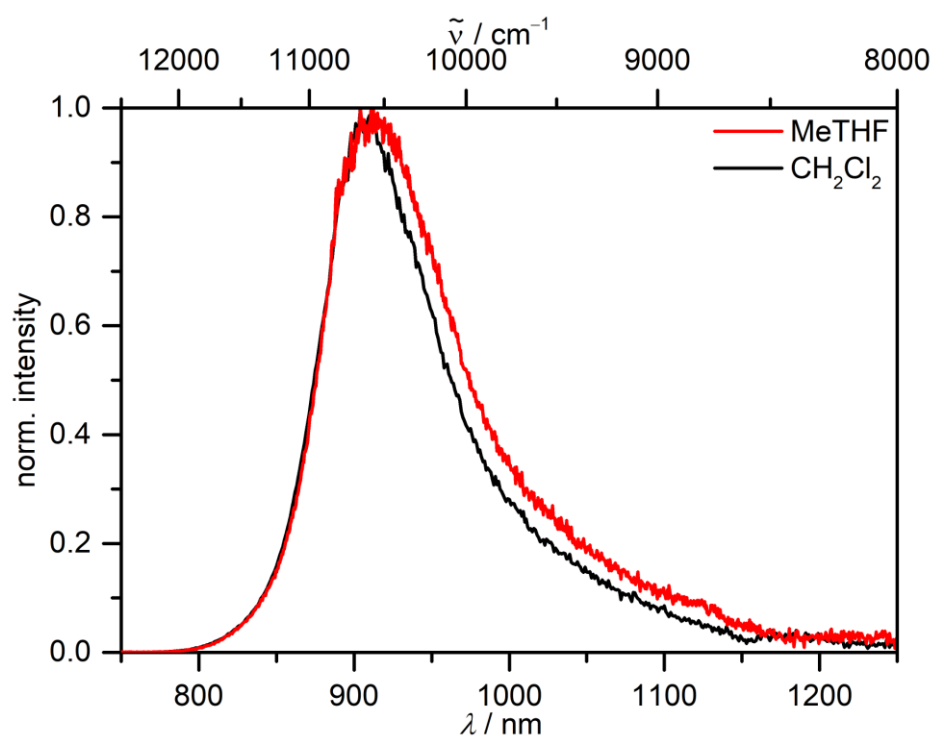


Figure S5. Emission spectra of *fac*-Cr(ppy)₃ in 2-MeTHF (red, $\lambda_{\text{exc}} = 420$ nm, scan slit width 10 nm) and CH₂Cl₂ (black, $\lambda_{\text{exc}} = 473$ nm, scan slit width 5 nm) at 293 K.

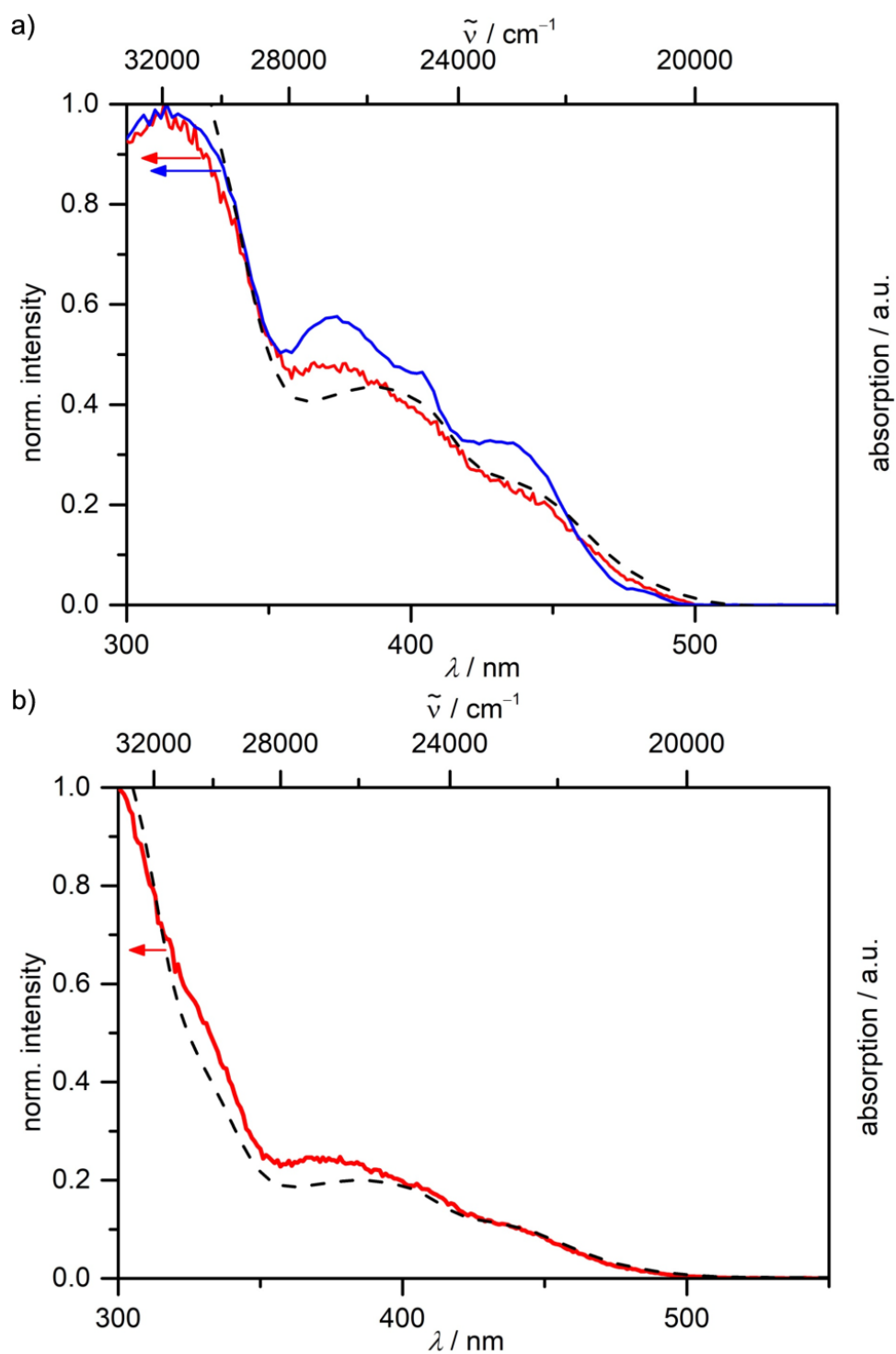


Figure S6. a) Absorption (black dotted line) and excitation spectra of *fac*-Cr(ppy)₃ in 2-MeTHF at 293 K (red, $\lambda_{\text{em}} = 880$ nm) and 77 K (blue, $\lambda_{\text{em}} = 890$ nm) and b) absorption (black dotted line) and excitation spectrum of *fac*-Cr(ppy)₃ in CH₂Cl₂ at 293 K (red, $\lambda_{\text{em}} = 870$ nm).

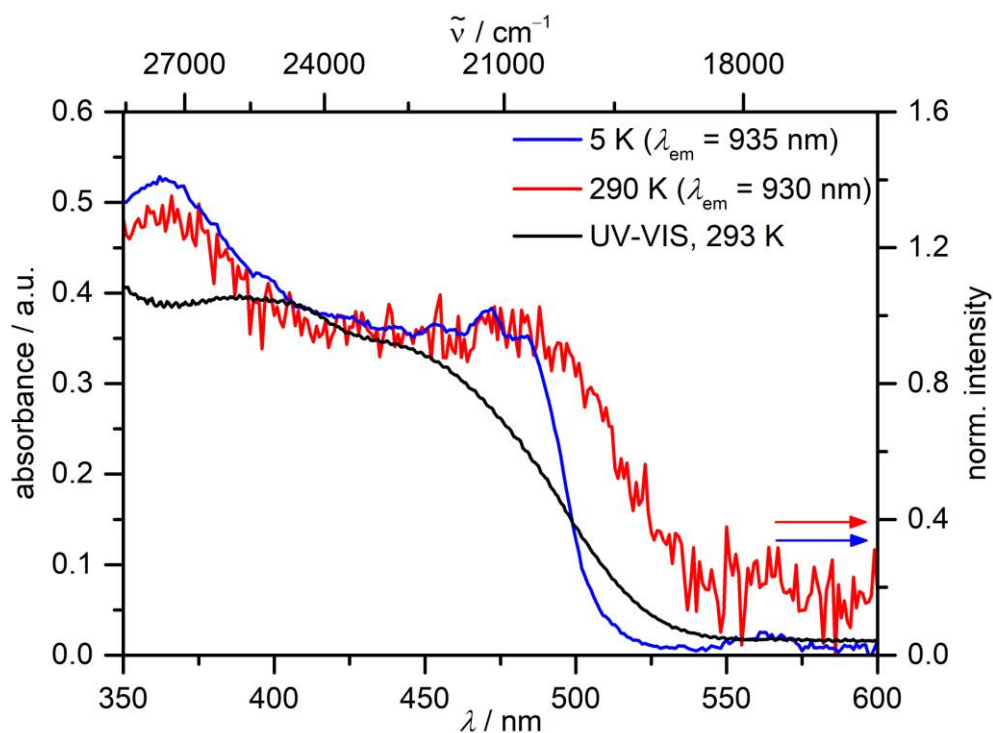


Figure S7. Absorption spectrum of *fac*-Cr(ppy)₃ as powder at 293 K (black) and excitation spectra of *fac*-Cr(ppy)₃ in a KBr pellet at 290 K (red, $\lambda_{\text{em}} = 930$ nm) and at 5 K (blue, $\lambda_{\text{em}} = 935$ nm).

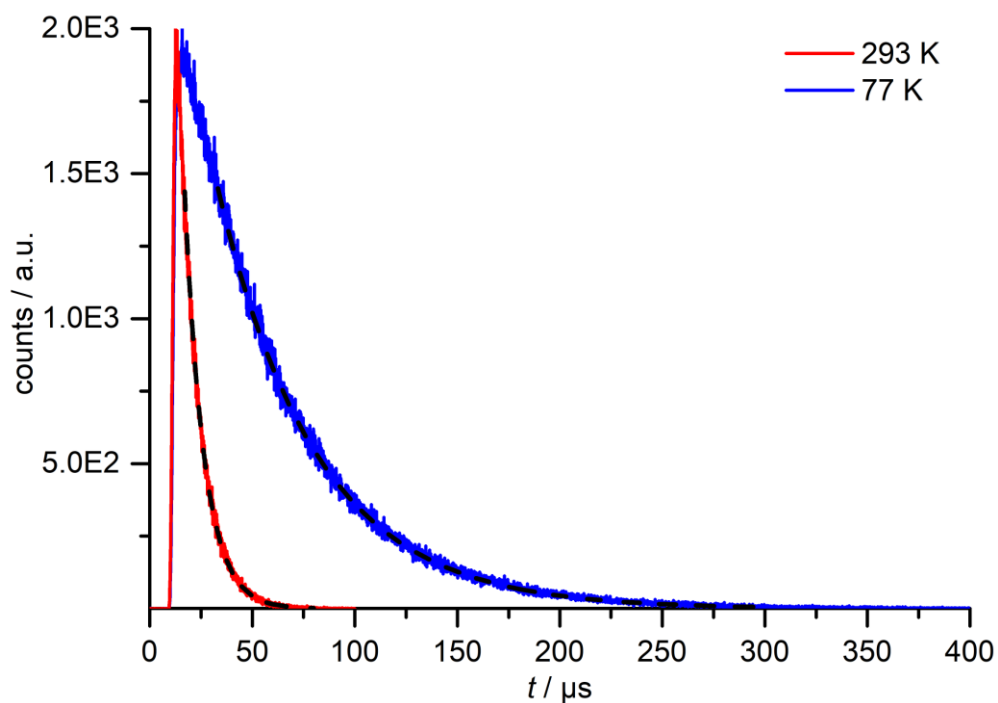


Figure S8. Lifetime scans of *fac*-Cr(ppy)₃ in 2-MeTHF at 77 K (blue, $\lambda_{\text{em}} = 890$ nm, $\lambda_{\text{exc}} = 420$ nm) and 293 K (red, $\lambda_{\text{em}} = 870$ nm, $\lambda_{\text{exc}} = 420$ nm). Applied monoexponential tailfits indicated as black dotted lines.

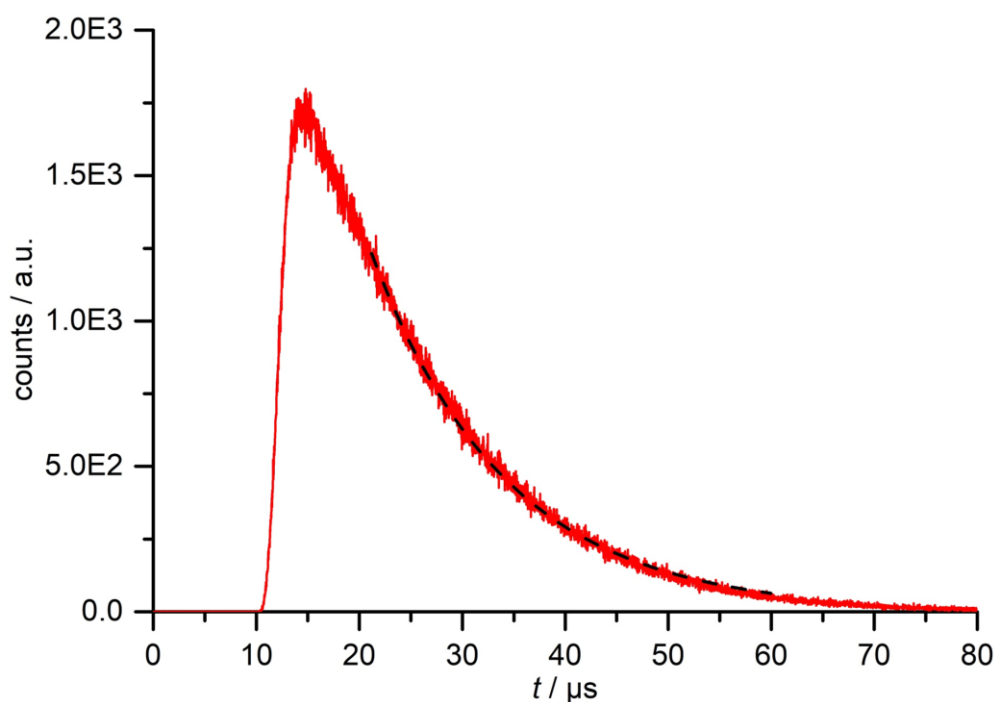


Figure S9. Lifetime scan of *fac*-Cr(ppy)₃ in CH₂Cl₂ at 293 K (red, $\lambda_{\text{em}} = 870$ nm, $\lambda_{\text{exc}} = 473$ nm). Applied monoexponential tailfit indicated as black dotted line.

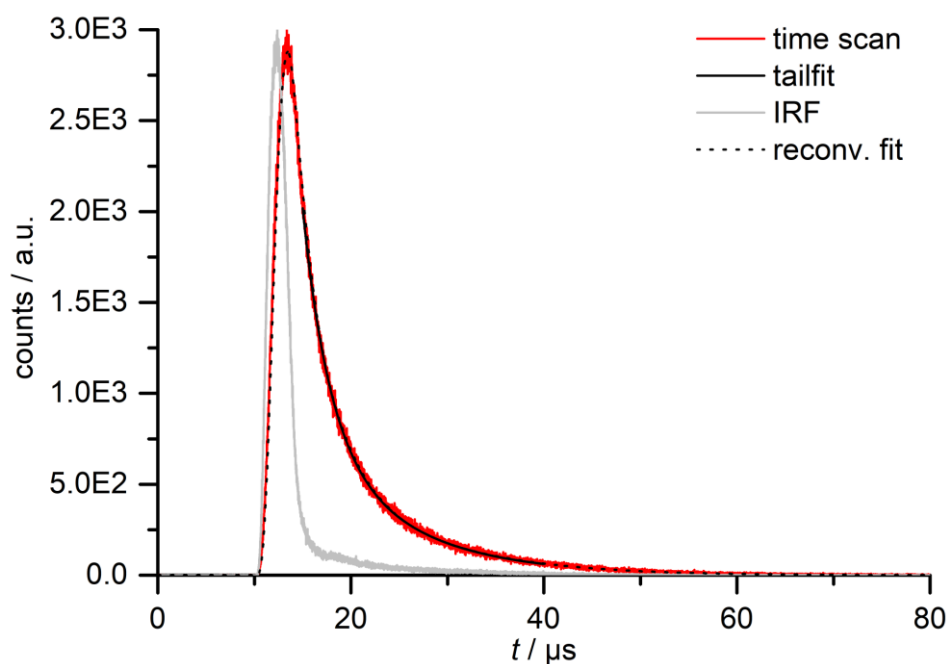


Figure S10. Lifetime scan (red) of solid *fac*-Cr(ppy)₃ at 293 K ($\lambda_{\text{em}} = 880$ nm). Tailfit and reconvolution fit (IRF in grey) indicated in black, solid and dotted, respectively. The lifetime in the solid state was determined with a biexponential tailfit as well as with a reconvolution fit including the IRF, resulting in the same output.

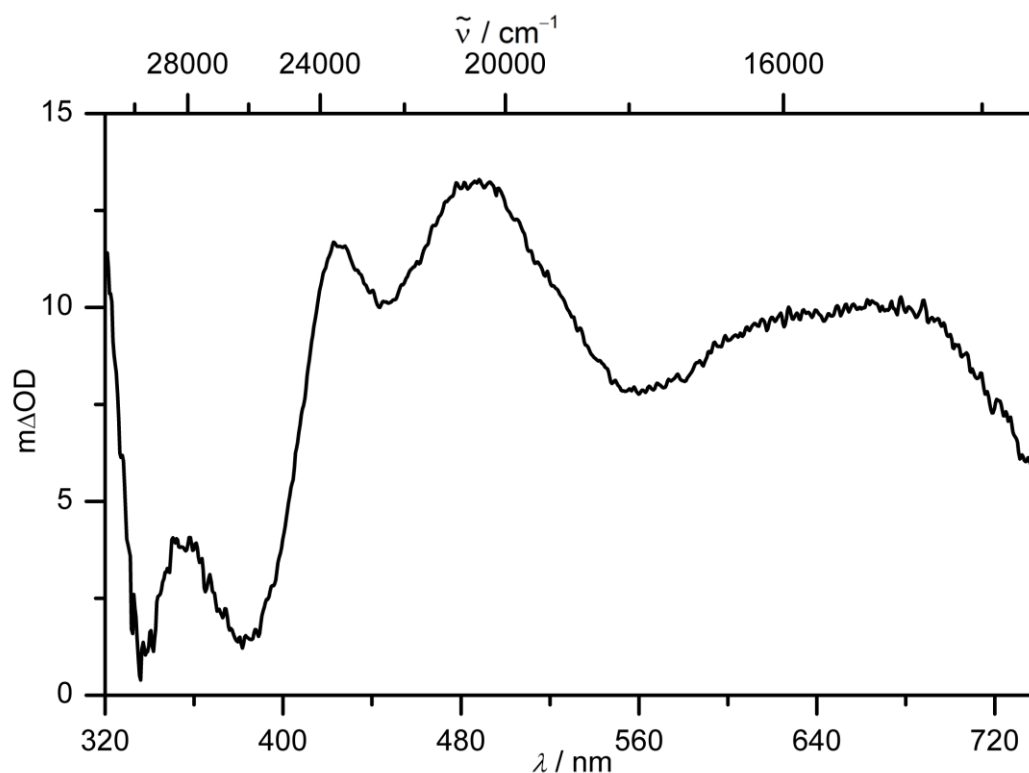


Figure S11. Transient absorption spectrum of *fac*-Cr(ppy)₃ in Ar-saturated CH₂Cl₂ at 293 K ($\lambda_{\text{exc}} = 355$ nm; ≈ 30 mJ pulse energy).

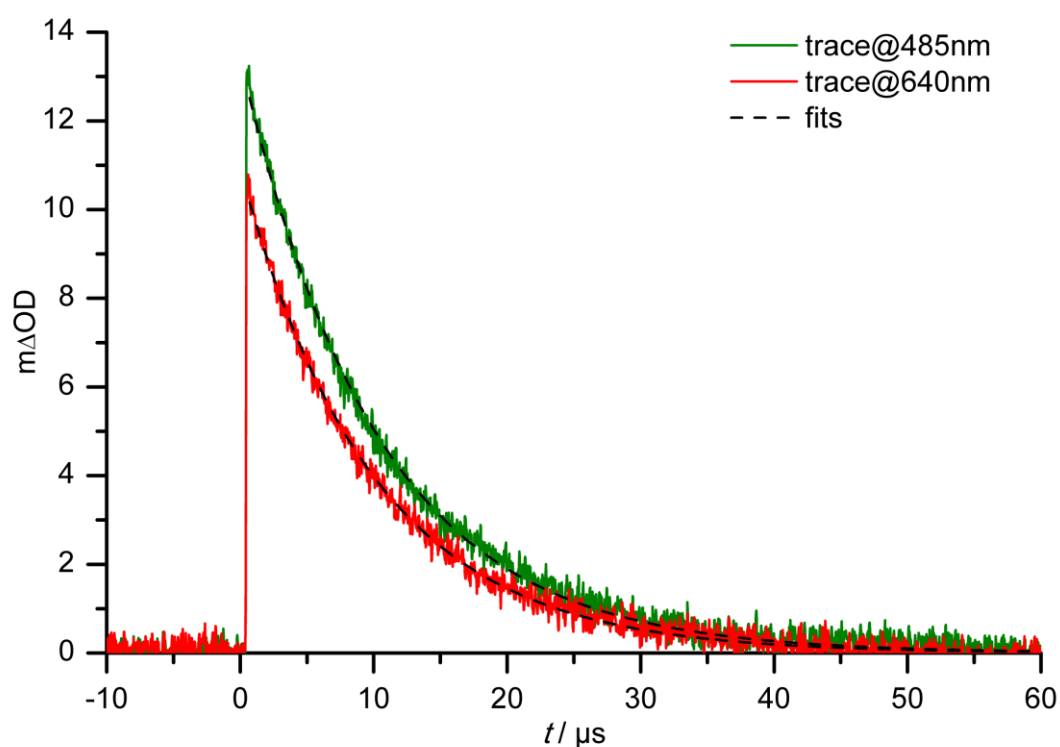


Figure S12. Transient absorption traces upon laser excitation ($\lambda_{\text{exc}} = 355$ nm; ≈ 30 mJ pulse energy) of *fac*-Cr(ppy)₃ in Ar-saturated CH₂Cl₂ at 293 K monitored at 485 nm (green) and at 640 nm (red). Applied monoexponential fits indicated as black dotted lines (485 nm: $y = 13.4082 \exp(-0.0977355 t)$; 640 nm: $y = 10.9038 \exp(-0.10069 t)$).

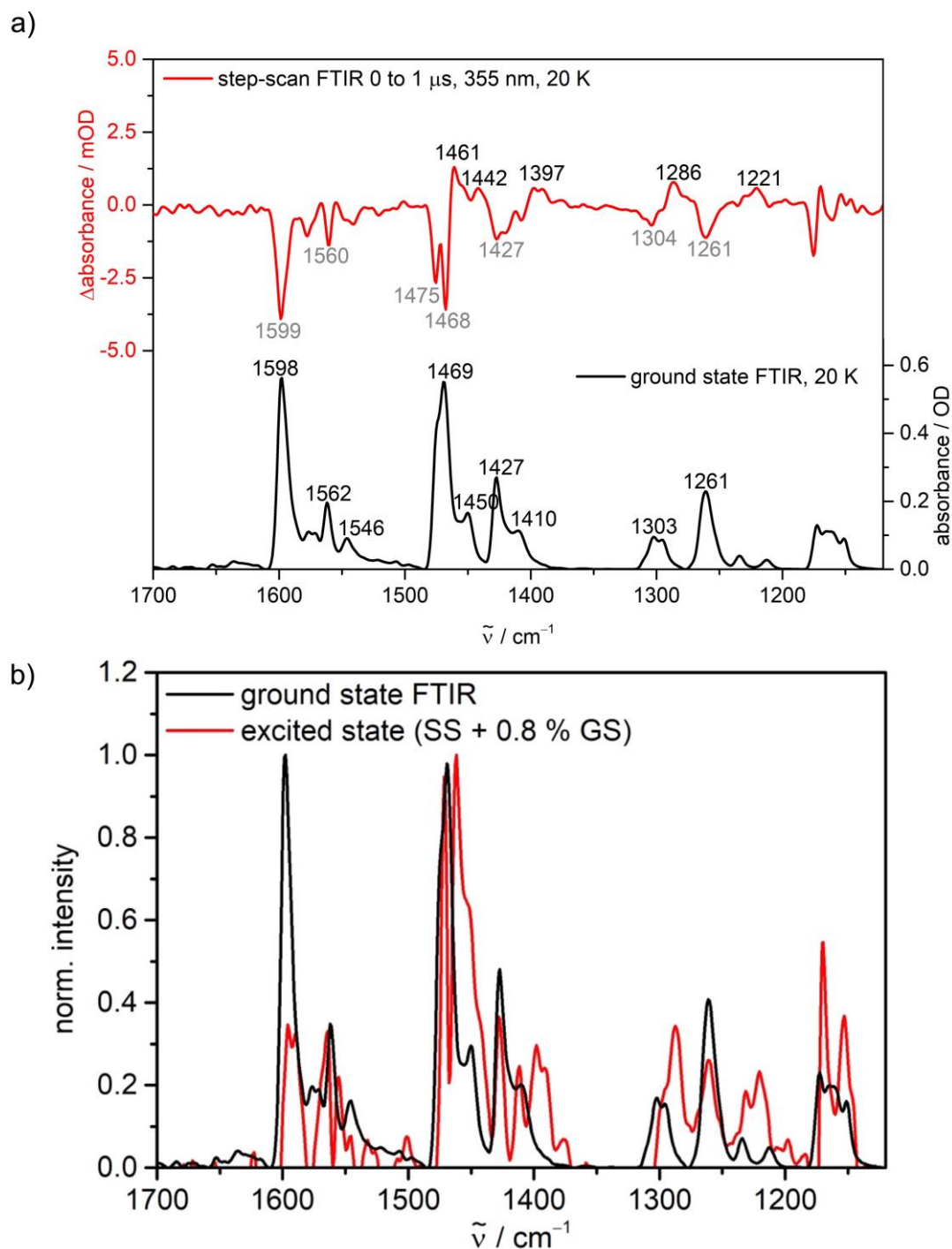


Figure S13. a) Step-scan difference spectrum (red, $\lambda_{\text{exc}} = 355$ nm) and ground state FTIR spectrum (black) of *fac*-Cr(ppy)₃ in the solid state (KBr matrix) at 20 K and b) ground state (black) and excited state (red, $\lambda_{\text{exc}} = 355$ nm) FTIR spectra of *fac*-Cr(ppy)₃ in a KBr pellet at 20 K. 0.8 % of the ground state spectrum was added to the step-scan difference spectrum to obtain the excited state spectrum.

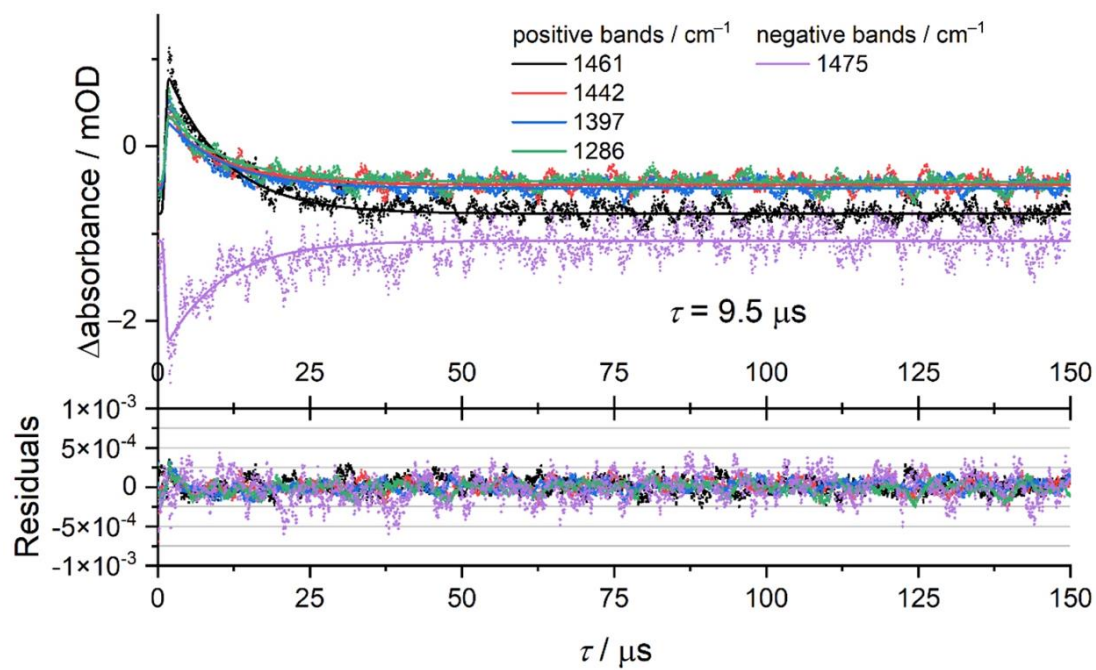


Figure S14. Global monoexponential fit applied to the decay curves of the most intense transient IR signals in the step-scan difference spectrum of *fac*-Cr(ppy)₃ at 20 K.

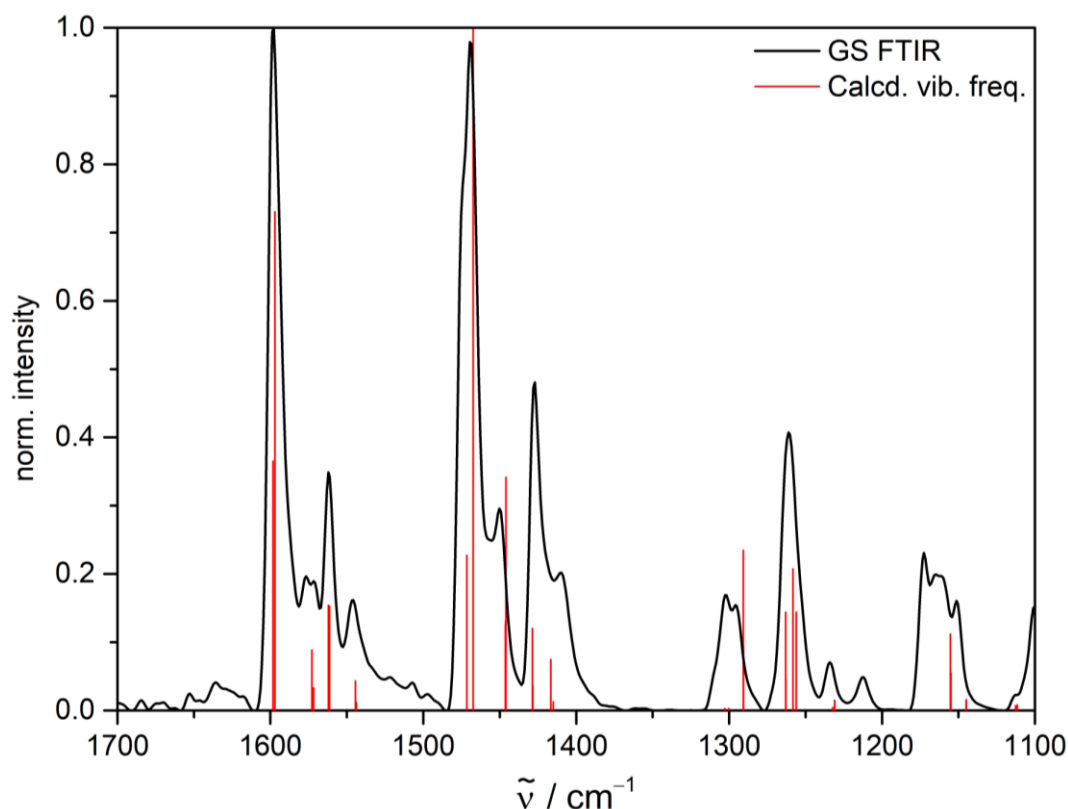


Figure S15. Ground state FTIR spectrum (black) of *fac*-Cr(ppy)₃ in the solid state (KBr matrix) at 20 K with calculated vibrational frequencies (scaled by 0.975) for the optimized ground state geometry of *fac*-Cr(ppy)₃.

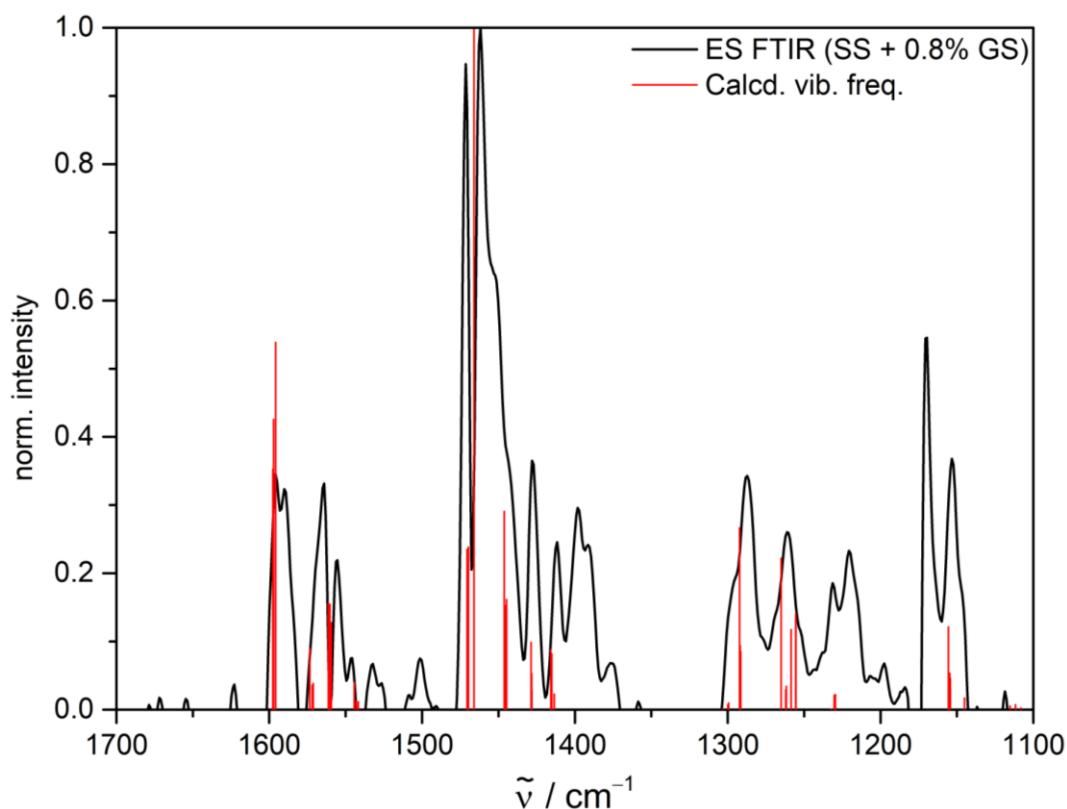


Figure S16. Step-scan difference spectrum (black, $\lambda_{\text{exc}} = 355$ nm) in the solid state (KBr matrix) at 20 K and calculated vibrational frequencies (scaled by 0.975) for the optimized doublet excited state geometry of *fac*-Cr(ppy)₃.

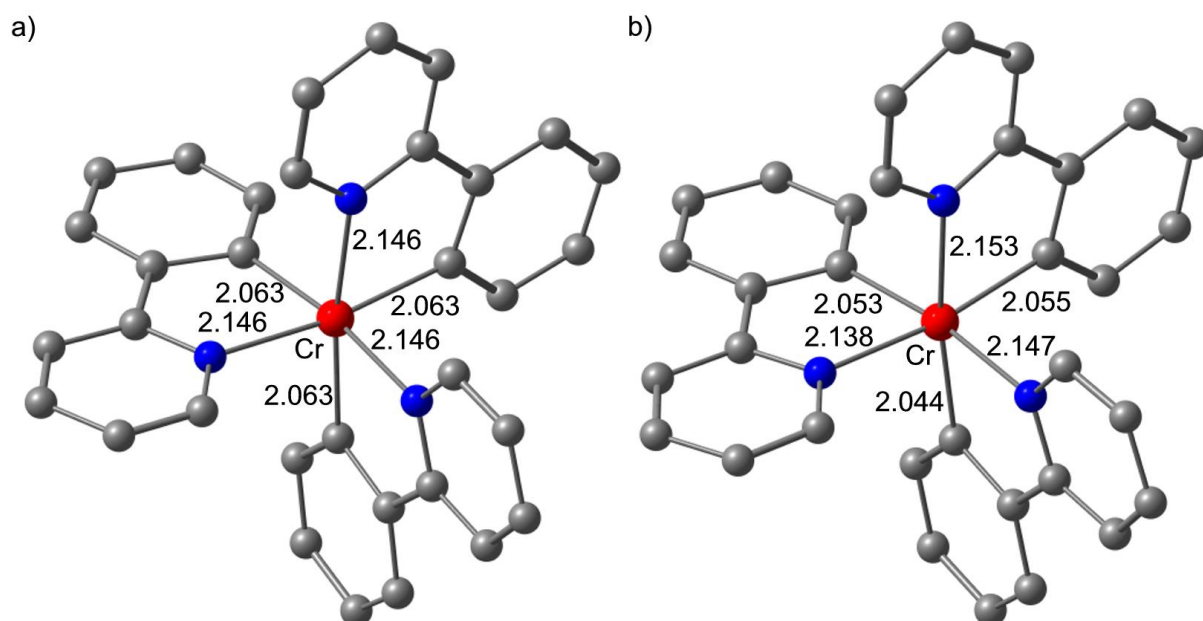


Figure S17. DFT optimized geometries of a) the quartet ground state and b) the lowest doublet state of *fac*-Cr(ppy)₃. The Mulliken spin densities at the chromium ion amount to 3.36 and 1.15, respectively.

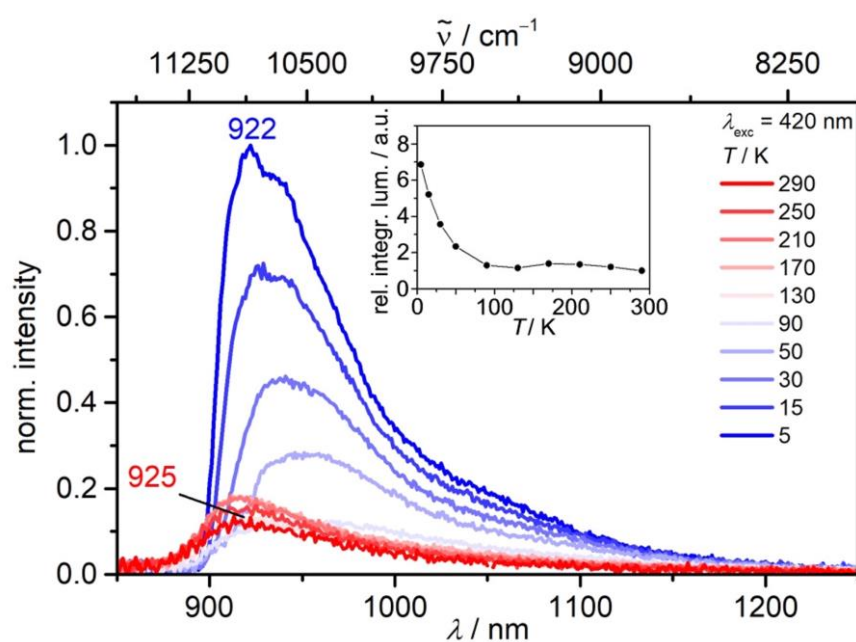


Figure S18. Emission spectra of *fac*-Cr(ppy)₃ in a KBr pellet at 290–5 K after excitation at 420 nm. The inset shows the corresponding relative integrated luminescence intensity vs. temperature plot.

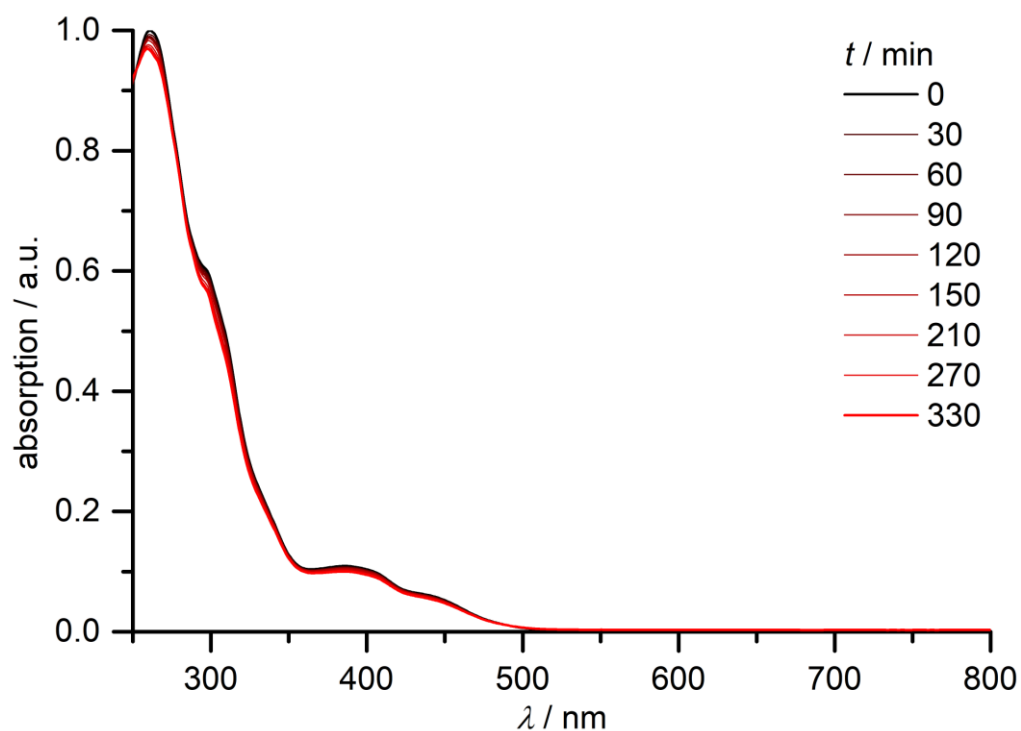


Figure S19. UV/Vis absorption spectra of *fac*-Cr(ppy)₃ in 2-MeTHF (saturated solution, ca. $c = 3.5 \times 10^{-5}$ M) during irradiation at 420 nm over time.

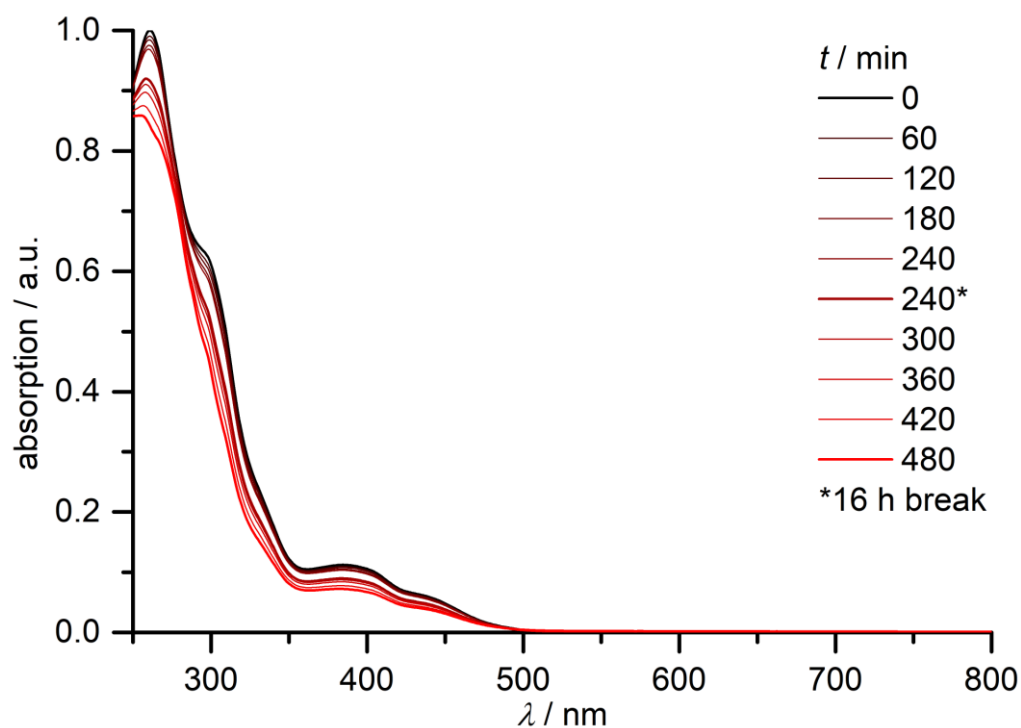


Figure S20. UV/Vis absorption spectra of *fac*-Cr(ppy)₃ in CH₂Cl₂ ($c = 5.3 \times 10^{-5}$ M) during irradiation at 420 nm over time.

Table S5. Cartesian Coordinates of calculated geometries of *fac*-Cr(ppy)₃ (quartet ground state and lowest doublet excited state) (CPCM(acetonitrile)-RIJCOSX B3LYP D3BJ ZORA-Def2-TZVPP).

	quartet ground state			doublet excited state		
Atom	X	Y	Z	X	Y	Z
24	-0.036293	-0.035312	-0.036011	-0.043552	-0.048731	-0.038663
7	-0.225446	0.017467	2.100852	-0.221295	0.017408	2.091302
6	-0.002051	0.160851	-2.089426	-0.003819	0.163327	-2.082253
6	-2.088967	0.009198	0.165139	-2.085305	-0.008136	0.167368
7	2.099565	-0.237552	0.011155	2.093836	-0.242996	0.010227
6	0.152484	-2.089344	0.001835	0.14849	-2.083656	-0.008841
7	0.02287	2.100887	-0.230501	0.014385	2.095754	-0.226253
6	1.490023	-2.548348	0.026738	1.48568	-2.550137	0.019689
6	0.788227	-0.001168	2.973209	0.796009	0.00977	2.961543
6	2.977999	0.770878	-0.006785	2.971821	0.766477	-0.004125
6	0.029725	2.54729	-1.509807	0.02987	2.547728	-1.503839
6	-3.074381	0.013221	-0.82821	-3.071853	-0.014363	-0.826083
6	0.029615	1.499881	-2.543593	0.031695	1.502401	-2.538348
6	-1.503664	0.028574	2.550283	-1.49825	0.035394	2.548916
6	-2.539877	0.038025	1.505318	-2.536693	0.031652	1.508012
6	0.01268	2.975704	0.781185	-0.000024	2.96819	0.787848
6	2.541244	-1.518478	0.017669	2.537701	-1.523706	0.017548
6	-0.006996	-0.834717	-3.0726	-0.006856	-0.832898	-3.066237
6	-0.846623	-3.068926	0.005544	-0.854651	-3.061992	-0.012922
6	-1.758683	0.024232	3.925164	-1.747006	0.05054	3.924428
6	0.59915	-0.004898	4.342888	0.612042	0.025262	4.331498
6	4.346501	0.573531	-0.014239	4.340255	0.569864	-0.006284
6	3.914549	-1.78178	0.009397	3.9112	-1.786037	0.015266
6	0.013925	4.344944	0.588893	0.006068	4.338002	0.599541
6	0.03023	3.921575	-1.768036	0.035948	3.922462	-1.758275
6	0.050699	1.810182	-3.910304	0.058559	1.811812	-3.904745
6	0.013124	-0.534962	-4.432763	0.018279	-0.533265	-4.426035
6	-3.905749	0.065113	1.818817	-3.902317	0.057792	1.821536
6	-4.433731	0.039308	-0.525274	-4.430606	0.011155	-0.522322
6	-0.551661	-4.430117	0.027783	-0.563833	-4.423225	0.004507
6	1.7955	-3.916111	0.050084	1.785153	-3.918842	0.039325
6	-4.852206	0.065278	0.804429	-4.848855	0.046802	0.807434
6	-0.706533	0.008563	4.823621	-0.691288	0.046736	4.818832
6	0.02345	4.822558	-0.717959	0.025269	4.820219	-0.705474
6	4.819327	-0.735057	-0.005478	4.814759	-0.738433	0.004501
6	0.775562	-4.856574	0.050129	0.761967	-4.855456	0.030917
6	0.041918	0.793671	-4.854433	0.051143	0.794998	-4.848474
1	-2.775284	0.030776	4.286399	-2.762451	0.063578	4.288907
1	1.781772	-0.012825	2.548945	1.788105	-0.008582	2.534633
1	1.449921	-0.018995	5.008177	1.466063	0.019375	4.9928
1	-0.90101	0.005458	5.887722	-0.88086	0.058865	5.883704
1	2.822003	-4.257985	0.06904	2.810643	-4.263576	0.061223

1	1.012159	-5.912484	0.067928	0.994239	-5.91233	0.045372
1	-1.351781	-5.161228	0.028189	-1.36673	-5.151237	-0.001682
1	-1.886517	-2.763401	-0.011378	-1.893127	-2.75296	-0.032947
1	-2.774947	-0.0066	-1.869818	-2.77267	-0.042438	-1.867446
1	-5.169584	0.03983	-1.321034	-5.166784	0.003287	-1.317711
1	-5.906647	0.085952	1.047269	-5.903307	0.066327	1.050262
1	-4.241677	0.086755	2.847261	-4.237462	0.08646	2.85009
1	-0.029256	-1.875573	-2.770715	-0.032015	-1.873364	-2.764127
1	0.006742	-1.332393	-5.166777	0.012821	-1.331182	-5.159497
1	0.057913	1.034029	-5.909524	0.071248	1.034755	-5.903609
1	0.074354	2.837781	-4.24863	0.085216	2.839476	-4.242658
1	4.269739	-2.800548	0.012265	4.266759	-2.80475	0.01967
1	5.882218	-0.93598	-0.011609	5.877905	-0.93803	0.003012
1	5.016889	1.420302	-0.027577	5.009932	1.417252	-0.016933
1	2.559746	1.767006	-0.014769	2.553004	1.762336	-0.013145
1	0.003883	2.553818	1.775768	-0.016032	2.544335	1.781347
1	0.006641	5.012267	1.438155	-0.004867	5.002456	1.451038
1	0.024154	5.886204	-0.914934	0.030284	5.884493	-0.898926
1	0.033745	4.280438	-2.785499	0.046841	4.283769	-2.774871

References

- 1 M. S. Wrighton, D. S. Ginley and D. L. Morse, *J. Phys. Chem.*, 1974, **78**, 2229–2233.
- 2 Y. S. Liu, P. de Mayo and W. R. Ware, *J. Phys. Chem.*, 1993, **97**, 5995–6001.
- 3 S. B. Meshkova, Z. M. Topilova, D. V. Bolshoy, S. V. Beltyukova, M. P. Tsvirko and V.Y. Venchikov, *Acta Phys. Pol. A*, 1999, **95**, 983–990.
- 4 STOE & Cie, X-Area, STOE & Cie GmbH, Darmstadt, Germany.
- 5 J. Koziskova, F. Hahn, J. Richter and J. Kožíšek, *Acta Chimica Slovaca*, 2016, **9**, 136–140.
- 6 STOE & Cie, X-Area LANA, STOE & Cie GmbH, Darmstadt, Germany.
- 7 G. M. Sheldrick, *Acta Crystallogr A Found Adv*, 2015, **71**, 3–8.
- 8 G. M. Sheldrick, *Acta Crystallogr C Struct Chem*, 2015, **71**, 3–8.
- 9 G. M. Sheldrick, *Acta Crystallogr C Struct Chem*, 2008, **64**, 112–122.
- 10 C. B. Hübschle, G. M. Sheldrick and B. Dittrich, *J Appl Crystallogr*, 2011, **44**, 1281–1284.
- 11 F. Neese, *WIREs Comput Mol Sci*, 2018, **8**.
- 12 A. D. Becke, *J. Chem. Phys.*, 1993, **98**, 5648–5652.
- 13 B. Miehllich, A. Savin, H. Stoll and H. Preuss, *Chem. Phys. Lett.*, 1989, **157**, 200–206.
- 14 F. Neese, F. Wennmohs, A. Hansen and U. Becker, *Chem. Phys.*, 2009, **356**, 98–109.
- 15 R. Izsák and F. Neese, *J. Chem. Phys.*, 2011, **135**, 144105.
- 16 D. A. Pantazis, X.-Y. Chen, C. R. Landis and F. Neese, *J. Chem. Theory Comput.*, 2008, **4**, 908–919.
- 17 S. Miertuš, E. Scrocco and J. Tomasi, *Chem. Phys.*, 1981, **55**, 117–129.
- 18 V. Barone and M. Cossi, *J. Phys. Chem. A*, 1998, **102**, 1995–2001.
- 19 A. Schäfer, H. Horn and R. Ahlrichs, *J. Chem. Phys.*, 1992, **97**, 2571–2577.
- 20 A. Schäfer, C. Huber and R. Ahlrichs, *J. Chem. Phys.*, 1994, **100**, 5829–5835.
- 21 S. Grimme, J. Antony, S. Ehrlich and H. Krieg, *J. Chem. Phys.*, 2010, **132**, 154104.
- 22 S. Grimme, S. Ehrlich and L. Goerigk, *J. Comput. Chem.*, 2011, **32**, 1456–1465.
- 23 S. Mai, F. Plasser, J. Dorn, M. Fumanal, C. Daniel and L. González, *Coord. Chem. Rev.*, 2018, **361**, 74–97.
- 24 F. Plasser, *J. Chem. Phys.*, 2020, **152**, 84108.
- 25 B. O. Roos, P. R. Taylor and P. E.M. Siegbahn, *Chem. Phys.*, 1980, **48**, 157–173.
- 26 P. E. M. Siegbahn, J. Almlöf, A. Heiberg and B. O. Roos, *J. Chem. Phys.*, 1981, **74**, 2384–2396.
- 27 C. Angeli, R. Cimiraglia, S. Evangelisti, T. Leininger and J.-P. Malrieu, *J. Chem. Phys.*, 2001, **114**, 10252–10264.
- 28 C. Angeli, R. Cimiraglia and J.-P. Malrieu, *J. Chem. Phys.*, 2002, **117**, 9138–9153.
- 29 K. Pierloot, *Int. J. Quantum Chem.*, 2011, **111**, 3291–3301.
- 30 W. Herwig and H. Zeiss, *J. Am. Chem. Soc.*, 1959, **81**, 4798–4801.
- 31 H. Dreves, *Z. Anorg. Allg. Chem.*, 1991, **605**, 145–150.
- 32 K. V. Goodwin, W. T. Pennington and J. D. Petersen, *Inorg. Chem.*, 1989, **28**, 2016–2018.
- 33 A. D. Kirk and G. B. Porter, *J. Phys. Chem.*, 1980, **84**, 887–891.
- 34 K. D. Barker, K. A. Barnett, S. M. Connell, J. W. Glaeser, A. J. Wallace, J. Wildsmith, B. J. Herbert, J. F. Wheeler and N. A.P. Kane-Maguire, *Inorg. Chim. Acta*, 2001, **316**, 41–49.
- 35 A. M. McDaniel, H.-W. Tseng, N. H. Damrauer and M. P. Shores, *Inorg. Chem.*, 2010, **49**, 7981–7991.